# A study of the energy deposition profile of proton beams in materials of hadron therapeutic interest

Rafael Garcia-Molina [a,*], Isabel Abril [b], Pablo de Vera [b], Ioanna Kyriakou [c], Dimitris Emfietzoglou [c]

[a] Departamento de Física, Centro de Investigación en Óptica y Nanofísica, Universidad de Murcia, E-30100 Murcia, Spain
[b] Departament de Física Aplicada, Universitat d'Alacant, E-03100 Alacant, Spain
[c] Medical Physics Laboratory, University of Ioannina Medical School, GR-45110 Ioannina, Greece

## HIGHLIGHTS

► The energy loss per unit path length by protons in liquid water, PMMA and polystyrene is calculated.
► We use a realistic description of the target excitation spectrum.
► Depth–dose curves of proton beams in these materials are obtained by using the simulation code SEICS.
► We obtain how the dose broadens radially as the depth increases.
► SEICS includes the main interaction phenomena between the projectile and the target constituents.

## ARTICLE INFO

## ABSTRACT

The energy delivered by a swift proton beam in materials of interest to hadron therapy (liquid water, polymethylmethacrylate or polystyrene) is investigated. An explicit condensed-state description of the target excitation spectrum based on the dielectric formalism is used to calculate the energy-loss rate of the beam in the irradiated materials. This magnitude is the main input in the simulation code SEICS (Simulation of Energetic Ions and Clusters through Solids) used to evaluate the dose as a function of the penetration depth and radial distance from the beam axis.

## 1. Introduction

The interaction of swift charged particles with different materials is currently used to gain insight into the structure of matter, as well as to characterize and modify the properties of the bombarded targets (Nastasi et al., 1998).

Besides the application to inert substances, the study of energetic projectiles interacting with materials of biological interest is also useful because they can be utilized in a controlled manner to kill malignant tumor cells, following the pioneering suggestion made by Wilson (1946).

The use of proton (or heavier ion) beams for treating tumors lies in the reduced amount of energy deposited into healthy tissue (as compared to photon or electron beam techniques) in contrast with the higher dose delivered at the tumor location, and the well defined range reached by the beam. Both characteristics are embodied in the depth–dose curve (commonly referred to as the Bragg curve), which represents the amount of energy delivered by the projectile as a function of the depth in the target.

Therefore, an accurate knowledge of the energy deposition profile (through the depth–dose curve and the spatial dispersion of the beam) is needed for an optimal application of treatment plannings in hadron therapy. It should be noticed that this is only the first step in a multiscale approach (Solov'yov et al., 2009) to a deeper understanding of the processes that are relevant for ion beam cancer therapy.

In Section 2 we summarize the formalism used to calculate, from the condensed matter point of view, the target stopping power and energy-loss straggling, which are the main features of the energy deposited by a proton beam in materials currently used in hadron therapy treatment planning, such as liquid water, polymethylmethacrylate (PMMA) or polystyrene (PS). These analytical results are employed in Section 3 as input into the simulation code SEICS, used to describe in detail the motion and the interactions of the beam particles through the bombarded target. In Section 4 we present and discuss our simulations for the

* Corresponding author. Fax: +34 868 888 568.
E-mail address: rgm@um.es (R. Garcia-Molina).

dose delivered as a function of the penetration depth (the Bragg curve) and also the radial distance to the beam axis. Finally, the conclusions of our work are drawn in Section 5.

## 2. Dielectric formalism of the energy loss by charged projectiles

The dielectric formalism (Lindhard, 1954; Ritchie, 1959) provides simple expressions for the most relevant magnitudes describing the electronic energy loss of a fast projectile (with mass $M$ and charge state $Q$) moving through matter with kinetic energy $E$, namely the stopping power $S_Q$ and the energy loss straggling $\Omega_Q^2$:

$$S_Q(E) = \frac{e^2 M}{\pi E} \int_0^\infty \frac{dk}{k} \rho_Q^2(k) \int_0^{k\sqrt{2E/M}} d\omega\, \omega \mathrm{Im}\left[\frac{-1}{\varepsilon(k,\omega)}\right], \quad (1)$$

$$\Omega_Q^2(E) = \frac{e^2 M\hbar}{\pi E} \int_0^\infty \frac{dk}{k} \rho_Q^2(k) \int_0^{k\sqrt{2E/M}} d\omega\, \omega^2 \mathrm{Im}\left[\frac{-1}{\varepsilon(k,\omega)}\right]. \quad (2)$$

The dependence upon the target properties is accounted for in these expressions through its energy-loss function (ELF) $\mathrm{Im}[-1/\varepsilon(k,\omega)]$, which is related to the probability that the projectile loses energy via an electronic excitation with momentum transfer $\hbar k$ and energy transfer $\hbar\omega$ to the target.

The projectile structure enters by means of the Fourier transform of its charge distribution, $\rho_Q(k)$, which is calculated according to the modified Brandt–Kitagawa model (Brandt and Kitagawa, 1982).

As a consequence of stochastic charge-exchange with the target electrons, the projectiles of a beam can be in different charge-states $Q$. Therefore, the stopping power $S$ and the energy-loss straggling $\Omega^2$ characterizing the energy lost by a beam of particles with atomic number $Z$ and with a given energy $E$ are expressed as a weighted sum over $S_Q(E)$ and $\Omega_Q^2(E)$, respectively,

$$S(E) = \sum_{Q=0}^{Z} \phi_Q(E) S_Q(E), \quad (3)$$

$$\Omega^2(E) = \sum_{Q=0}^{Z} \phi_Q(E) \Omega_Q^2(E), \quad (4)$$

where the charge-state fractions, $\phi_Q(E)$, which do not only depend on the projectile energy, but also on its nature as well as on the target characteristics, are obtained from a parameterization to the experimental equilibrium charge fractions (Schiwietz and Grande, 2001).

Among various semi-empirical computational schemes (Emfietzoglou et al., 2009; Garcia-Molina et al., 2012) for modeling the ELF, the MELF-GOS (Mermin Energy Loss Function-Generalized Oscillator Strength) method (Abril et al., 1998; Heredia-Avalos et al., 2005) yields a realistic description of the target excitation spectrum over the whole energy-momentum space for a broad range of materials (metals, insulators, semiconductors, and biomaterials), provided experimental optical data are available.

In this work we will be concerned with materials of biological interest, such as liquid water, PMMA and PS, which are frequently used in hadron therapy treatment plans as tissue phantoms. In Fig. 1 we show, by symbols, the experimental optical ELF ($k=0$) of liquid water (Hayashi et al., 2000), PMMA (Ritsko et al., 1978) and PS (Inagaki et al., 1977), where the corresponding fitting with the MELF-GOS model (lines) is also included. The MELF-GOS methodology makes a separation of the ELF into outer and inner electronic excitation contributions (Abril et al., 1998; Heredia-
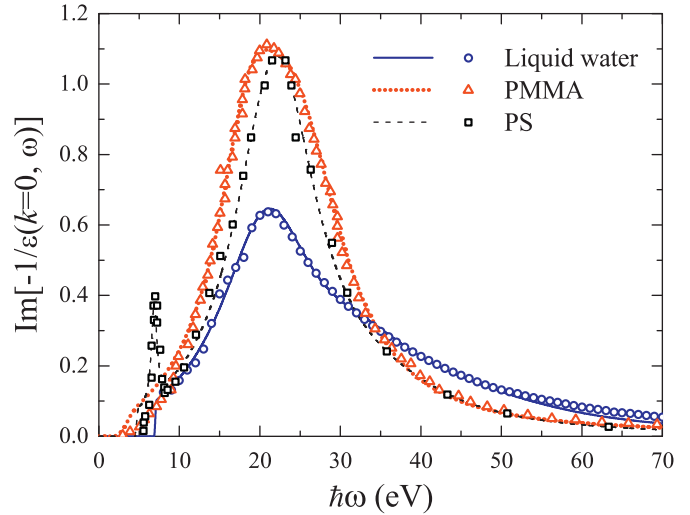


**Fig. 1.** Experimental energy loss function, $\mathrm{Im}[-1/\varepsilon(k=0,\omega)]$, of liquid water (circles) (Hayashi et al., 2000), PMMA (triangles) (Ritsko et al., 1978) and PS (squares) (Inagaki et al., 1977) in the optical limit ($k=0$). Lines correspond to the fit by the MELF-GOS model.

**Table 1**
Fitting parameters $A_i$, $\hbar\omega_i$ and $\hbar\gamma_i$ used in the MELF-GOS model for liquid water, PMMA and PS. $\hbar\omega_{\mathrm{th},i}$ is the threshold energy appearing in Eq.(5).

| Target | $i$ | $\hbar\omega_i$ (eV) | $\hbar\omega_i$ (eV) | $A_i$ | $\hbar\omega_{\mathrm{th},i}$(eV) |
|---|---|---|---|---|---|
| Liquid water | 1 | 22.0 | 14.00 | 0.23 | 7 |
| | 2 | 34.0 | 19.00 | 0.131 | |
| | 3 | 47.0 | 31.97 | 1.15 | |
| PMMA | 1 | 19.14 | 9.07 | 0.128 | 3 |
| | 2 | 25.36 | 14.41 | 0.395 | |
| | 3 | 70.75 | 48.98 | 0.030 | |
| PS | 1 | 6.88 | 0.68 | 0.002 | 4.6 |
| | 2 | 22.86 | 12.25 | 0.390 | |
| | 3 | 36.74 | 21.77 | 0.080 | |

Avalos et al., 2005),

$$\mathrm{Im}\left[\frac{-1}{\varepsilon(k,\omega)}\right] = \mathrm{Im}\left[\frac{-1}{\varepsilon(k,\omega)}\right]_{\mathrm{outer}} + \mathrm{Im}\left[\frac{-1}{\varepsilon(k,\omega)}\right]_{\mathrm{inner}}$$

$$= \sum_i A_i \mathrm{Im}\left[\frac{-1}{\varepsilon_{\mathrm{M}}(\omega_i,\gamma_i;k=0,\omega)}\right] \Theta(\omega-\omega_{\mathrm{th},i})$$

$$+ \frac{2\pi^2 \mathcal{N}}{\omega} \sum_{n\ell} \frac{df_{n\ell}(k,\omega)}{d\omega} \quad (5)$$

where, in order to include condensed target effects, the outer electron contribution to the ELF is fitted to the experimental optical ELF by a weighted sum of Mermin-type ELF (Mermin, 1970). In the above expression $\varepsilon_{\mathrm{M}}$ is the Mermin dielectric function, $A_i$, $\omega_i$ and $\gamma_i$ are, respectively, the intensity, position and width of each Mermin-type ELF, $\hbar\omega_{\mathrm{th},i}$ is a threshold energy; all these values are presented in Table 1 for the different materials discussed in this paper. The inner-shell electrons are described by their generalized oscillator strengths (GOS) in the hydrogenic approach, where $df_{n\ell}(k,\omega)/d\omega$ is the GOS of the $(n,\ell)$ sub-shell and $N$ is the molecular density of the target. The recompense of this model is that if one fits the ELF to the experimental data at $k=0$, due to the analytical dependence of the Mermin dielectric function with the momentum transfer, it is not necessary to assume any extension algorithm to obtained the Bethe surface. Another important quantity that can be obtained with the MELF-GOS model is the mean excitation energy $I$ of the target, whose values are 79.4 for liquid water (Garcia-Molina et al., 2009),
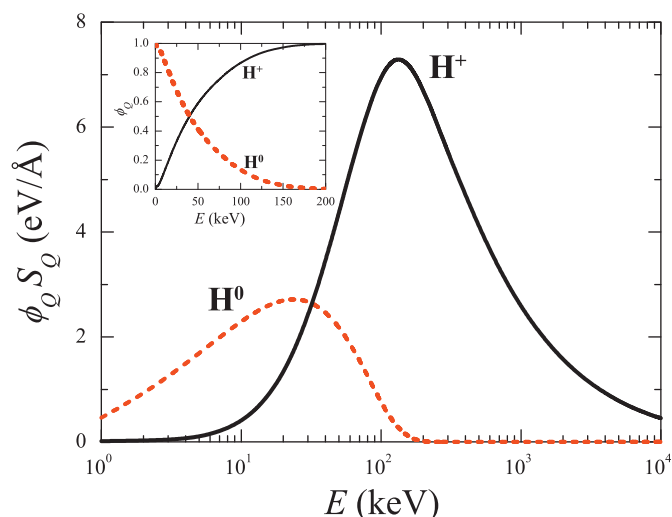
**Fig. 2.** Weighted contribution to the stopping power of liquid water due to each charge fraction, $\phi_0(E)S_0(E)$ and $\phi_1(E)S_1(E)$, for hydrogen projectiles (dashed line) and protons (solid line), respectively, as a function of the projectile energy. The inset shows the charge fractions of $H^0$ (dashed line) and $H^+$ (solid line) in water (Schiwietz and Grande, 2001).



**Fig. 3.** Stopping power of liquid water (solid line), PMMA (dotted line) and PS (dashed line), as a function of the proton beam energy, calculated from the dielectric formalism and the MELF-GOS model.

70.3 for PMMA (de Vera et al., 2011) and 72.1 eV for PS. From the ICRU report the recommended *I*-values are 78 eV for liquid water (Sigmund et al., 2009), $74 \pm 1.5$ eV for PMMA (ICRU37, 1984) and 72.5 eV for PS (ICRU49, 1992).

We study the energy deposition in biological materials, such as liquid water, PMMA and PS, by swift proton beams in the energy range of tens of MeV. Although the energies used in hadron therapy are larger, beam projectiles reach the Bragg peak (where most effectiveness is needed) with much lower energies. Besides, the charge-state fractions $\phi_Q$ of $H^+$ and $H^0$ in water depicted in the inset of Fig. 2 show that the proportion of $H^0$ projectiles grows as the energy decreases. A similar behavior appears for the other biomaterials discussed in this work because of their similar constitution by light elements (Abril et al., 2013). The stopping power of liquid water (weighted by the corresponding charge-state fractions) appearing in Fig. 2 shows that neutral hydrogen projectiles $H^0$ begin to be important in the energy loss processes at energies lower than around 100 keV. Therefore, the distinct contribution to the dose delivered by $H^0$ and $H^+$ must be adequately considered when a detailed description of the interactions taking place around and at the distal part of the Bragg peak is desired.

In Fig. 3 we present the stopping power *S*, Eq. (3), for protons as a function of their incident energy of several materials currently used when planning hadron therapy treatments (liquid water, PMMA and PS). It is interesting to notice that their maximum values take place at almost the same proton energies, i.e. around 100 keV, because the ELFs of these materials have a main single peak at $\sim$20 eV. The different stopping powers of these materials, and especially the significantly larger value for PMMA at the maximum (for 100 keV the stopping powers of liquid water, PS and PMMA are 7.75, 8.61 and 10.1 eV/Å, respectively) is caused by differences in the shape and magnitude of their electron excitation spectrum, their chemical composition and molecular density.[1] Therefore these differences must be taken into account when using liquid water, PMMA or PS in dosimetry measurements. The energy loss at high proton energies
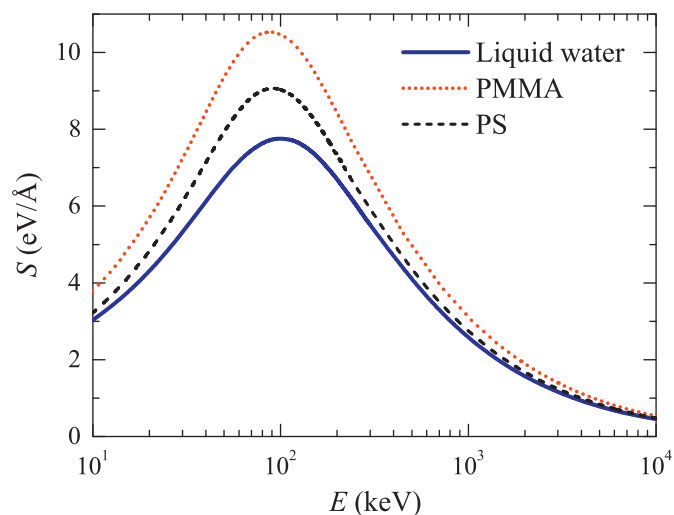
is given correctly by the relativistic Bethe equation (Inokuti, 1971), which mainly depends on the mean excitation energy *I* of the target.

Proceeding in a similar manner to the previous discussion for the stopping power, we obtain from Eq. (4) the proton energy-loss straggling $\Omega^2$ for liquid water, PMMA, and PS, which is depicted in Fig. 4; the value of $\Omega^2$ is a measure of the fluctuation in the energy loss of the projectile due to the inelastic interactions with the electrons of the target. The sizeable differences that appear between the values of $\Omega^2$ for PMMA, PS and liquid water in the whole proton energy range are due to the different contribution to the ELF from both the outer-electron excitation spectrum and the inner-shell electron excitation. At high proton energies, the energy-loss straggling can be calculated analytically by the relativistic form of the Bohr energy-loss straggling.

## 3. Simulation of the beam particles motion through the target

The energy deposited by energetic protons in targets of biological interest, as well as the spatial and energy distributions of the beam as a function of the depth is simulated by means of the SEICS code (Simulation of Energetic Ions and Clusters through Solids). A detailed description of the program is given by Garcia-Molina et al. (2011); here, a summary of the main features of the SEICS code are presented.

We use Molecular Dynamics to follow in detail the motion of the projectiles through the target, and a Monte Carlo procedure to treat the statistical nature of the elastic and inelastic scattering as well as the charge-exchange processes between the projectile and the target electrons.

The trajectory of each projectile through the stopping medium is obtained by numerically solving its equation of motion. Given the instantaneous position $\vec{r}(t)$, velocity $\vec{v}(t)$ and force $\vec{F}(t)$ acting on the particle at a given time *t*, its new position $\vec{r}(t+\Delta t)$ and velocity $\vec{v}(t+\Delta t)$ after a time step $\Delta t$, are obtained by using the velocity variant of Verlet's algorithm, with the relativistic character of the projectile being taken into account. The force $\vec{F}(t)$ that slows down the energetic particle traveling with charge-state *Q* through the target takes into account the stochastic nature of the inelastic (electronic) energy loss processes, so it is obtained from a randomly sampled Gaussian distribution with mean value $S_Q$ and variance $\Omega_Q^2/(v\Delta t)$. The values of $S_Q$ and $\Omega_Q^2$ are

---

[1] An incorrect drawing of the stopping power of PMMA for low energy protons (Abril et al., 2013) is properly plotted in Fig. 3.

obtained from the dielectric formalism, together with the MELF-GOS model, as previously described.

Electron capture and loss processes by the projectile are also included in the simulation through a Monte Carlo scheme, so the energy loss dependence with the projectile charge-state $Q$ is properly taken into account according to the description provided in the preceding paragraph.

Finally, the simulation also considers multiple elastic scattering between the target nuclei and the projectile resulting in its angular deflection (i.e., lateral spreading) and, at the end of its travel, an appreciable contribution to the projectile energy-loss. The multiple elastic scattering between the projectile and the target nuclei is described by the universal interatomic potential (Ziegler et al., 2008).

Some representative results provided by the simulation (depth–dose profile, spatial distribution and mean value of the projectile charge-state) are depicted schematically in Fig. 5 for a 10 MeV proton beam moving through liquid water and PMMA. We have considered these two materials because they show the maximum differences in their electronic stopping power, as can be seen in Fig. 3. We observe in Fig. 5 the spatial dispersion of the paths followed by the projectiles, which deposit most of their energy at the end of their trajectories (at the Bragg peak), as depicted by the color code associated to the stopping power.
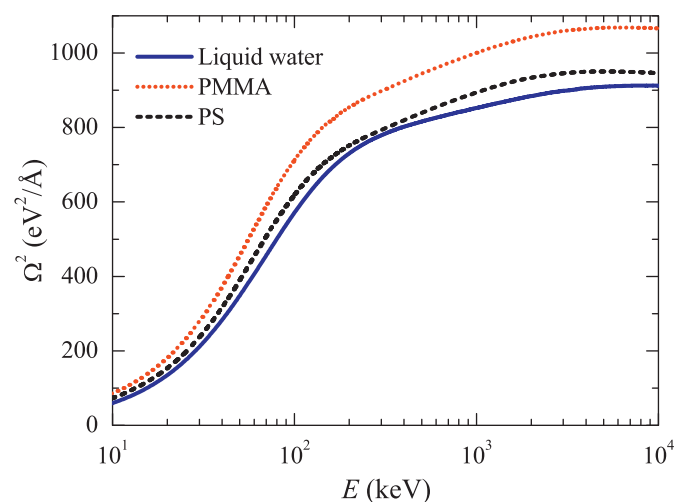
The dotted curve, showing the average charge state of the beam as a function of the target depth, indicates that the projectiles are mainly protons until reaching the Bragg peak, where (due to their low energy) electrons are captured to form $H^0$, according to the results presented in the inset of Fig. 2. Differences between the proton trajectories in liquid water and PMMA, as well as in the position of the Bragg peak (solid gray line), can be clearly observed in Fig. 5, which indicate that a proton beam deposits its energy in a rather different manner in these materials.

## 4. Results and discussion

In this section we summarize and discuss the main results obtained with the simulation code SEICS for proton beams interacting with liquid water, PMMA and PS. The depth–dose curves for these materials are shown in Fig. 6 for a proton beam having 10 MeV. We can see how the different stopping powers and energy-loss stragglings of these materials give rise to differences in the depth–dose curves, mainly in the position and intensity of the Bragg peak. PMMA has a shorter range and a more intense Bragg peak than the other materials (as a consequence of having a larger stopping power), whereas the deeper depth–dose profile corresponds to liquid water.
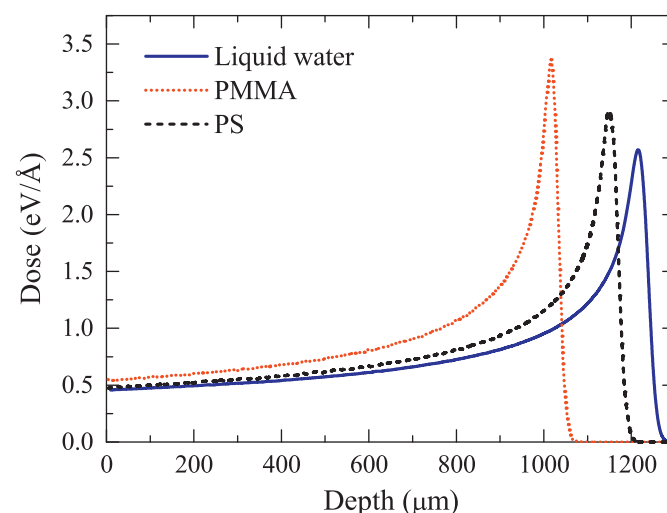


**Fig. 4.** Calculated energy loss-straggling of liquid water (solid line), PMMA (dotted line) and PS (dashed line), as a function of the proton beam energy, obtained from the dielectric formalism and the MELF-GOS model.



**Fig. 6.** Depth–dose distribution of a 10 MeV proton beam in liquid water (solid line), PMMA (dotted line) and PS (dashed line) obtained with the SEICS code.
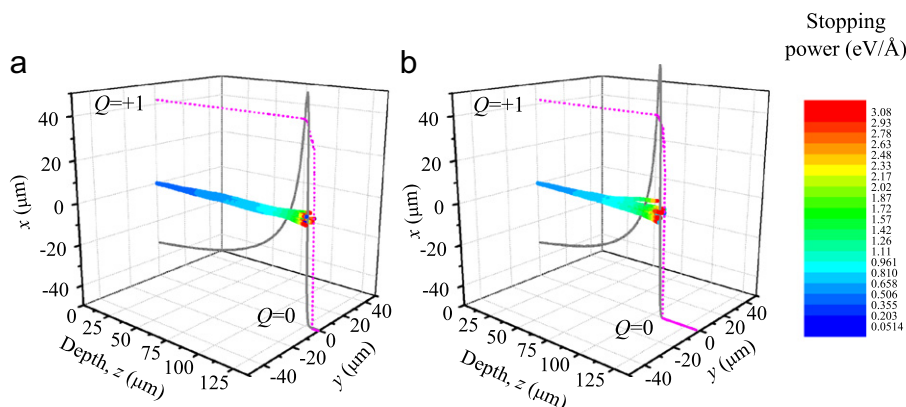


**Fig. 5.** Simulated depth–dose distribution (gray solid line), projectile spatial distribution (colored lines according to the value of the stopping power) and average value of the charge state (magenta dotted line) for a 10 MeV proton beam interacting with (a) liquid water and (b) PMMA. Only a few trajectories have been plotted to simplify the picture. (For interpretation of the references to color in this figure legend, the reader is referred to the web version of this article.)

The depth–dose curve quantifies the energy delivered by the proton beam at a given depth $z$ from the target entrance, but as the scattered trajectories depicted in Fig. 5 suggest, part of this energy may be deposited at a radial distance from the beam axial direction. Since the simulation code SEICS follows the trajectory of each projectile, the energy delivered at each position (not only at a given depth) can be tracked in detail.

In Fig. 7 we show the root mean square radius $\langle r^2 \rangle^{1/2}$ of the beam, representing its lateral dispersion due to multiple elastic collisions, as a function of the depth in liquid water for 5 MeV, 10 MeV and 100 MeV proton beams. For comparison purposes we also show in Fig. 7 the corresponding depth–dose distributions (gray solid lines) (multiplied by 0.2 and 7, respectively for the 5 MeV and 100 MeV proton beams). We have found from the
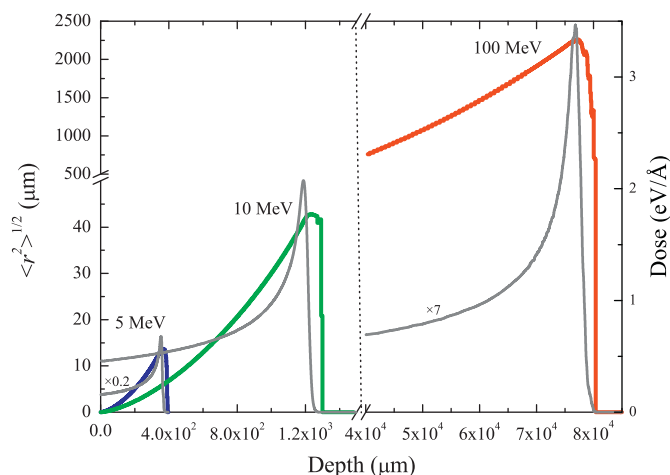
simulation that $\langle r^2 \rangle^{1/2}$ increases with the depth, following a parabolic dependence, and suddenly falls down at the distal part of the Bragg peak. This latter feature happens because only a few projectiles travel in almost straight line to reach these deeper regions, whereas most of the projectiles, that undergo nuclear elastic scattering, deviate from their initial direction and stop at lower depths.

Following the evolution of the radial broadening of the proton beam with the depth in liquid water, depicted in Fig. 7, we obtain the important result that at the Bragg peak position the root mean square radius of the projectile spatial distribution is ∼3% of the beam range, independently of the incident energy of the beam. This fact indicates that a sizeable part of the beam energy is delivered at regions perpendicular to the place tumor position where the beam is aimed. At proton energies of 10 MeV the spread of the beam at the Bragg peak is only several tens of microns. But at the typical proton energies used in hadron therapy (hundreds of MeV), the dispersion of the beam will reach several millimeters at the Bragg peak, where the maximum dose is deposited in the target. Therefore, an accurate knowledge of the beam lateral deviation is of crucial importance when preparing the hadron therapy treatments, in order to achieve an effective delivery of energy to the malignant cells with minimum damage to the surrounding healthy tissue.

As the SEICS code accurately simulates the trajectories of the beam projectiles, the energy deposited in the target is known as a function of the spatial coordinates. Therefore, for each depth $z$ we can obtain the energy delivered at a radial distance $r$ from the axial (i.e., incident) direction, which represent the distribution of energy perpendicular to the beam entrance direction. In Fig. 8, to visualize the lateral spreading of the deposited energy with respect to the Bragg curve, we define $\Phi(z,r) = \Phi(z)(N(z,r))/(N(z,r=0))$, where $\Phi(z)$ is the dose at a given depth $z$ (that is, the Bragg curve, Fig. 6), and $N(z,r)$ represents the number of particles at a given depth $z$ and at given radial distance $r$. Note that the projection of the Bragg curve corresponds to $r=0$, but $\Phi(z,r)$ is only a pictorial representation of the energy spreading
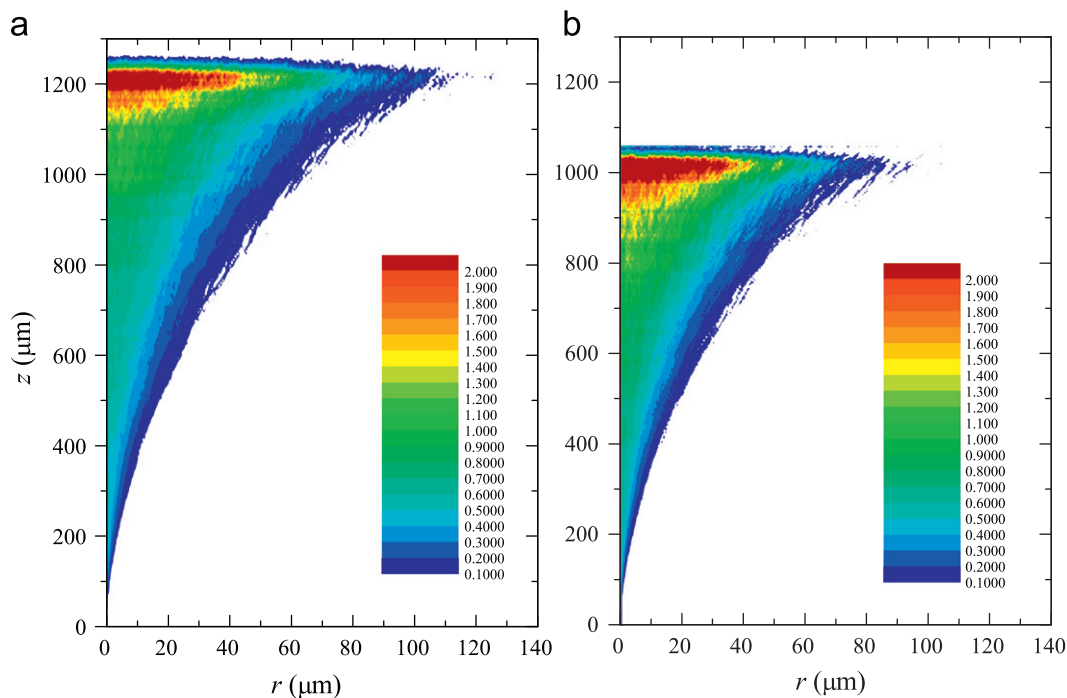


**Fig. 7.** (Left axis) Root mean square radius of the beam (thick solid lines) as a function of the depth for 5 MeV, 10 MeV and 100 MeV proton beams incident in liquid water, obtained with the SEICS code. (Right axis) The corresponding depth–dose distributions (gray thin lines) are shown for comparison; the depth–dose distributions for 5 MeV and 100 MeV protons are scaled by 0.2 and 7 respectively.



**Fig. 8.** Dose deposited $\Phi(z,r)$ by a 10 MeV proton beam as a function of the depth $z$ and the radial distance $r$ to the initial beam direction for (a) liquid water and (b) PMMA. See the text for more details. (For interpretation of the references to color in this figure legend, the reader is referred to the web version of this article.)

when moving far from the entrance axis. It can be seen, due to multiple elastic scattering, that the radial spreading of the delivered dose grows as the depth increases. The greater concentration of deposited energy takes place along the beam entrance axis ($r=0$), with the maximum (darker red area) being located at the Bragg peak, but the lateral spreading of this energy is not negligible, specially around the Bragg peak where it reaches ∼8% of the range.

The information depicted in Fig. 8 also clearly shows the distinct depth and radial distribution of the energy deposited in liquid water and PMMA. The former (liquid water) having larger values of the position of the Bragg peak as compared with PMMA due to its smaller stopping power. On the other hand, PMMA ($C_5H_5O_2)_n$ presents a bigger radial broadening of the beam compared with liquid water ($H_2O$) at the same depth, due to its larger interatomic (screened Coulomb) potential for elastic collisions. However, as the range of the protons in liquid water is larger than for PMMA, those protons continue undergoing multiple elastic collisions in the target until they are stopped. Therefore, the larger radial broadening of the beam at the Bragg peak in liquid water in comparison with PMMA, is only due to the fact that the protons in liquid water travel more distance than in PMMA.

## 5. Conclusions

In this work we have presented the simulated depth–dose and spatial profiles of proton beams in several materials of interest in hadron therapy, such as liquid water, PMMA and PS. These results have been obtained with the SEICS (Simulation of Energetic Ions and Clusters through Solids) code, which is based in a combination of Monte Carlo and Molecular Dynamics techniques to follow in detail the trajectories of each projectile through the target, taking into account inelastic (electronic) interactions, multiple elastic scattering and charge exchange processes.

A condensed matter point of view has been used to properly describe the target electronic excitation spectrum, which plays a main role in the energy loss processes, quantified through the stopping power and the energy-loss straggling. The different features of the Bragg curves (position, intensity and shape) for each material are mainly consequence of their different stopping magnitudes. The deeper Bragg peak of liquid water, compared to PS and PMMA, being a consequence of having the smaller stopping power of the three materials discussed in this work.

We have also evaluated the root mean square radius of the beam cross section which behaves as a parabola as a function of the depth $z$. Our simulations confirm that at the Bragg peak, the maximum average radial distance is around 3% of the Bragg peak depth, whereas the energy delivered extends to around 8%, independent of the target and the energy of the incident beam. These results indicate that for proton beams with energy of several hundreds of MeV, which are currently used in hadron therapy, the broadening of the incident beam can reach several millimeters.

## Acknowledgments

## References

Abril, I., Garcia-Molina, R., Denton, C.D., Pérez-Pérez, F.J., Arista, N.R., 1998. Dielectric description of wakes and stopping powers in solids. Phys. Rev. A 58, 357–366.

Abril, I., Garcia-Molina, R., de Vera, P., Kyriakou, I., Emfietzoglou, D., Inelastic collisions of energetic protons in biological media. In: Belkic, Dz. (Ed.). Adv. Quant. Chem. 65 (2013) 129-164.

Brandt, W., Kitagawa, M., 1982. Effective stopping-power charges of swift ions in condensed matter. Phys. Rev. B 25, 5631–5637.

de Vera, P., Abril, I., Garcia-Molina, R., 2011. Inelastic scattering of electron and light ion beams in organic polymers. J. Appl. Phys. 109, 094901–094908.

Emfietzoglou, D., Garcia-Molina, R., Kyriakou, I., Abril, I., Nikjoo, H., 2009. A dielectric response study of the electronic stopping power of liquid water for energetic protons and a new I-value for water. Phys. Med. Biol. 54, 3451–3472.

Garcia-Molina, R., Abril, I., Denton, C.D., Heredia-Avalos, S., Kyriakou, I., Emfietzoglou, D., 2009. Calculated depth-dose distributions for $H^+$ and $He^+$ beams in liquid water. Nucl. Instrum. Methods B 267, 2647–2652.

Garcia-Molina, R., Abril, I., Heredia-Avalos, S., Kyriakou, I., Emfietzoglou, D., 2011. A combined molecular dynamics and Monte Carlo simulation of the spatial distribution of energy deposition by proton beams in liquid water. Phys. Med. Biol. 56, 6457–6493.

Garcia-Molina, R., Abril, I., Kyriakou, I., Emfietzoglou, D., 2012. Energy loss of swift protons in liquid water: role of optical data input and extension algorithms. In: García Gómez-Tejedor, G., Fuss, M.C. (Eds.), Radiation Damage in Biomolecular Systems. Springer, Dordrecht, pp. 239–262. (Chapter 15).

Hayashi, H., Watanabe, N., Udagawa, Y., Kao, C.C., 2000. The complete optical spectrum of liquid water measured by inelastic X-ray scattering. Proc. Nat. Acad. Sci. USA 97, 6264–6266.

Heredia-Avalos, S., Garcia-Molina, R., Fernández-Varea, J.M., Abril, I., 2005. Calculated energy loss of swift He, Li, B, and N ions in $SiO_2$, $Al_2O_3$ and $ZrO_2$. Phys. Rev. A 72 052902-1–9.

ICRU37, 1984. Stopping Powers for Electrons and Positrons. ICRU Report Vol. 37, International Commission on Radiation Units and Measurements, Bethesda, MD, USA.

ICRU49, 1992. Stopping Powers and Ranges for Protons and Alpha Particles. ICRU Report Vol. 49, International Commission on Radiation Units and Measurements, Bethesda, MD, USA.

Inagaki, T., Arakawa, E.T., Hamm, R.N., Williams, M.W., 1977. Optical properties of polystyrene from the near-infrared to the X-ray region and convergence of optical sum rules. Phys. Rev. B 15, 3243–3253.

Inokuti, M., 1971. Inelastic collisions of fast charged particles with atoms and molecules: the Bethe theory revisited. Rev. Mod. Phys. 43, 297–347.

Lindhard, J., 1954. On the properties of a gas of charged particles. Dan. Mat. Fys. Medd. 28, 8.

Mermin, N.D., 1970. Lindhard dielectric function in the relaxation-time approximation. Phys. Rev. B 1, 2362–2363.

Nastasi, M., Mayer, J.W., Hirvonen, J.K., 1998. Ion–Solid Interactions: Fundamentals and Applications. Cambridge University Press, Cambridge.

Ritchie, R.H., 1959. Interaction of charged particles with a degenerate Fermi–Dirac electron gas. Phys. Rev. 114, 644–654.

Ritsko, J.J., Brillson, L.J., Bigelow, R.W., Fabish, T.J., 1978. Electron energy loss spectroscopy and the optical properties of polymethylmethacrylate from 1 to 300 eV. J. Chem. Phys. 69, 3931–3939.

Schiwietz, G., Grande, P.L., 2001. Improved charge-state formulas. Nucl. Instrum. Methods Phys. Res. B 175–177, 125–131.

Sigmund, P., Schinner, A., Paul, H., 2009. Errata and Addenda for ICRU Report 73, Stopping of Ions Heavier Than Helium, International Commission on Radiation Units and Measurements, Bethesda, MD, USA.

Solov'yov, A.V., Surdutovich, E., Scifoni, E., Mishustin, I., Greiner, W., 2009. Physics of ion beam cancer therapy: a multiscale approach. Phys. Rev. E 79 011909-1–7.

Wilson, R.R., 1946. Radiological use of fast protons. Radiology 47, 487–491.

Ziegler, J.F., Biersack, J.P., Ziegler, M.D., 2008. SRIM. The Stopping and Range of Ions in Matter. Chester, MD: SRIM Co.